J. Fluid Mech. (1972), *vol.* 55, *part* 3, *pp.* 493–511
Printed in Great Britain

A nonlinear analysis of pulsatile flow in arteries

By S. C. LING AND H. B. ATABEK

Department of Aerospace and Atmospheric Sciences, The Catholic University of America, Washington, D.C.

(Received 1 March 1972)

An approximate numerical method for calculating flow profiles in arteries is developed. The theory takes into account the nonlinear terms of the Navier–Stokes equations as well as the nonlinear behaviour and large deformations of the arterial wall. Through the locally measured values of the pressure, pressure gradient and pressure–radius function the velocity distribution and wall shear at a given location along the artery can be determined. The computed results agree well with the corresponding experimental data.

1. Introduction

The study of blood flow in arteries has occupied the attention of the researchers for over 150 years. Like most of the problems of life sciences, it is a complex one and has defied all attempts at a completely satisfactory solution. Mathematical treatment of the problem has been subjected to constant changes and modifications to account for new evidence uncovered through improved experimental measurements. One can trace the history and development of the problem from numerous review articles. The most consistent treatment of the problem was given by Womersley (1957). Later, his analysis was extended by others to include the effect of initial stresses, perivascular tethering and orthotropic and viscoelastic behaviour of the arterial wall. A detailed comparison of this group of articles is given by Cox (1969).

Womersley's theory and its extensions are based on the linearized Navier–Stokes equations and small elastic deformations. Although they are shown to be satisfactory in describing certain aspects of the flow in small arteries, they fail to give an adequate representation of the flow field, especially in large arteries, see Fry, Griggs & Greenfield (1964) and Ling, Atabek & Carmody (1969). Because of the large dynamic storage effect of these arteries, the nonlinear convective acceleration terms of the Navier–Stokes equations are no longer negligible. Moreover, the walls of arteries undergo large deformations. As a result of this, both the geometric and elastic nonlinear effects come into play, see Ling (1970).

To take these factors into account an approximate numerical method is developed. The method, assuming axially symmetric flow, predicts the velocity distribution and wall shear at a given location in terms of locally measured values of the pressure, pressure gradient and pressure–radius relation. The results of computations show good agreement with the corresponding experimental

data. The simplicity of the method may make it useful in circulatory research, where detailed flow characteristics are required under a wide range of arterial pressures and heart rates.

2. Statement of the problem

Pulse propagation phenomena in arteries are caused by the interaction of blood with the elastic arterial wall. Therefore, the mathematical statement of the problem should include equations which govern the motion of blood and the motion of the arterial wall, and also the relations (boundary conditions) which connect these two motions with each other. This set of equations and conditions make a formidable boundary-value problem. However, the problem can be greatly simplified through the following three experimental observations.

(i) The radial motion of the arterial wall is primarily dictated by the pressure wave.

(ii) The perivascular tethering has a strong dampening effect on the longitudinal motion of the arterial wall, hence this motion may be neglected, see Patel, Greenfield & Fry (1964).

(iii) To a large extent velocity profiles are developed locally as the pressure wave propagates along the artery, hence they do not carry a significant amount of momentum history from far upstream. This somewhat unusual behaviour of the flow can be explained in terms of the combined effects of fast propagation of the pressure wave and large distensibility and taper of the arterial wall. For example, during systole, the heart of a medium-sized dog ejects approximately 25 ml of blood into the ascending aorta. Assuming that the cross-sectional area of the root of the aorta during systole to be 4·5 cm^2, the corresponding displacement of the blood along the aorta will be only 5·5 cm. During this time a fast-rising pressure-gradient wave front, approximately 12 cm in width, accelerates blood locally as it sweeps along the aorta with a speed of $\sim$ 400 cm/s. As a result, in most parts of the aorta, the momentum boundary layer is developed locally with a minor contribution from the preceding cardiac cycles. This momentum layer is significantly reduced by the local convective accelerations which are generated through both the natural taper of the vessel and taper due to the wave front. In addition, the radial velocity of the flow near the expanding wall will generate a similar effect. These two latter effects will be discussed in detail in § 4.3. After closure of the aortic valve, blood in the root of aorta is essentially at rest. At distal locations, the overall passive contraction of the arterial wall will create a basic flow which will be increasing with distance owing to the integration of wall flux. The magnitude of this diastolic flow is small and, as before, the momentum boundary layer is developed locally and is reduced by the local convective acceleration due to arterial taper. Thus, within a cardiac cycle, the mean momentum defect produced by the mean wall shear is effectively absorbed by the mean positive convective accelerations. For this reason, little information about the flow is convected far downstream, and the entrance effect is essentially confined to a displacement distance corresponding to one heart beat. The asymmetrical velocity profiles created by an arterial branch are found to be confined

to a distance of 10 diameters, which is again approximately equal to the displacement length of blood for one heart beat, see Ling, Atabek & Carmody (1969). Similarly, asymmetrical velocity profiles and secondary flows developed by the aortic arch and arterial branches are found to be localized and are not convected into the descending aorta.

The first two of the above observations will permit one to decouple the motion of the arterial wall from the motion of the blood, while the third observation will allow one to simplify the equations governing the motion of blood.

2.1. *Equations governing the motion of blood*

For this problem blood can be taken as an incompressible Newtonian fluid. We shall use the cylindrical co-ordinates r, θ and z, with z along the axis of the vessel. Since our aim is to use locally measured quantities to predict the local flow characteristics, the choice of the origin of z is immaterial.

The motion of blood is governed by the Navier–Stokes equations and the equation of continuity. We shall assume that the flow is axially symmetric and body forces are absent. Under these assumptions the governing equations have the following form:

$$\frac{\partial u}{\partial t}+u\frac{\partial u}{\partial r}+w\frac{\partial u}{\partial z}=-\frac{1}{\rho}\frac{\partial p}{\partial r}+\nu\left(\frac{\partial^2 u}{\partial r^2}+\frac{1}{r}\frac{\partial u}{\partial r}+\frac{\partial^2 u}{\partial z^2}-\frac{u}{r^2}\right), \tag{1}$$

$$\frac{\partial w}{\partial t}+u\frac{\partial w}{\partial r}+w\frac{\partial w}{\partial z}=-\frac{1}{\rho}\frac{\partial p}{\partial z}+\nu\left(\frac{\partial^2 w}{\partial r^2}+\frac{1}{r}\frac{\partial w}{\partial r}+\frac{\partial^2 w}{\partial z^2}\right), \tag{2}$$

$$\frac{\partial u}{\partial r}+\frac{u}{r}+\frac{\partial w}{\partial z}=0. \tag{3}$$

Here t denotes time, u and w denote the components of the fluid velocity in the r and z directions, respectively, p is the pressure, ρ is the density and ν is the kinematic viscosity of blood.

2.2. *Motion of the arterial wall*

As is indicated above, the longitudinal motion of the arterial wall is significantly arrested by the perivascular tethering. Here we shall neglect this component of the arterial motion and seek a simple relation connecting local values of the radial pressure force, mass and elastic response of the arterial wall. Let $R = R(z, t)$ denote the inner radius of the artery. We assume that the variation of R with pressure is known (determined experimentally). Let us denote this functional relation by $p = P(R)$. Although the effect of arterial taper (both the natural taper and the generated taper due to the wave front) on the motion of blood is important because of convective acceleration, its effect on the radial motion of artery is negligible. Therefore the equation of motion for the arterial wall can be written as

$$\frac{m}{2\pi R}\frac{\partial^2 R}{\partial t^2}=p(z,t)-P(R). \tag{4}$$

Here m denotes the effective mass of the artery per unit length in its natural state. Equation (4) is valid only locally (for a fixed z) and to emphasize this point we

use the partial derivative with respect to time. With p known as a function of time and the local elastic response of an artery, starting with homogeneous initial conditions, one can integrate this equation numerically to determine R as a function of time.

2.3. *Simplification of the equation of motion*

Equation (2) may be simplified by dropping the term $\partial^2 w/\partial z^2$, which is negligible in comparison with the radial derivatives. Because of the small radial velocity and acceleration, the radial variation of pressure within the artery can also be neglected. Therefore the longitudinal pressure gradient $\partial p/\partial z$ may be considered as a function of z and t only. Let us take $-\rho^{-1}(\partial p/\partial z) = F(z,t)$. Hereafter, we shall assume that $F(z,t)$ is an experimentally determined, known function. Then (2) may be written as

$$\frac{\partial w}{\partial t}+u\frac{\partial w}{\partial r}+w\frac{\partial w}{\partial z} = F(z,t)+\nu\left(\frac{\partial^2 w}{\partial r^2}+\frac{1}{r}\frac{\partial w}{\partial r}\right). \tag{5}$$

As a result of the replacement of $\partial p/\partial z$ with a known function, (5) now contains only two unknown dependent variables, u and w. Equation (3) also contains only these dependent variables. Therefore, these two equations together are sufficient to determine both u and w. Of course we have to supplement them with proper boundary and initial conditions. In the radial direction the boundary conditions are

$$u(r,z,t)|_{r=R(z,t)} = \partial R/\partial t, \tag{6}$$

$$w(r,z,t)|_{r=R(z,t)} = 0, \tag{7}$$

$$[\partial w(r,z,t)/\partial r]_{r=0} = 0. \tag{8}$$

Boundary conditions in the z direction reflect the effect of upstream and downstream flows on the local flow. Since the aim is to determine the local flow from the locally measured flow properties, it is necessary to find a way to eliminate the need for boundary conditions on z. This will be accomplished, later, by eliminating all explicit z dependence from the equations.

Since the first two boundary conditions given above are prescribed at a moving surface, the problem is difficult to handle. However, by introducing the coordinate transformation

$$\eta = r/R(z,t) \tag{9}$$

we can rewrite the boundary conditions as

$$u(\eta,z,t)|_{\eta=1} = \partial R/\partial t, \tag{10}$$

$$w(\eta,z,t)|_{\eta=1} = 0, \tag{11}$$

$$[\partial w(\eta,z,t)/\partial \eta]_{\eta=0} = 0. \tag{12}$$

Carrying the transformation (9) into (5) and (3) we obtain

$$\frac{\partial w}{\partial t}-\left(\frac{\eta}{R}\frac{\partial R}{\partial t}-\frac{u}{R}\right)\frac{\partial w}{\partial \eta}+w\left(\frac{\partial w}{\partial z}-\frac{\eta}{R}\frac{\partial R}{\partial z}\frac{\partial w}{\partial \eta}\right) = F(z,t)+\frac{\nu}{R^2}\left(\frac{\partial^2 w}{\partial \eta^2}+\frac{1}{\eta}\frac{\partial w}{\partial \eta}\right) \tag{13}$$

and

$$\frac{1}{R}\frac{\partial u}{\partial \eta}+\frac{u}{\eta R}+\frac{\partial w}{\partial z}-\frac{\eta}{R}\frac{\partial R}{\partial z}\frac{\partial w}{\partial \eta} = 0. \tag{14}$$

By solving (14) for $\partial w/\partial z$ and substituting it into (13) we can eliminate explicit z dependence from this equation:

$$\frac{\partial w}{\partial t} = F(z,t) + \left(\frac{\eta}{R}\frac{\partial R}{\partial t} - \frac{u}{R}\right)\frac{\partial w}{\partial \eta} + \frac{w}{R}\left(\frac{\partial u}{\partial \eta} + \frac{u}{\eta}\right) + \frac{\nu}{R^2}\left(\frac{\partial^2 w}{\partial \eta^2} + \frac{1}{\eta}\frac{\partial w}{\partial \eta}\right). \tag{15}$$

On integrating (14) with respect to η between zero and η we find that

$$u = \frac{\partial R}{\partial z}\eta w - \frac{2}{\eta}\frac{\partial R}{\partial z}\int_0^\eta \eta w\, d\eta - \frac{R}{\eta}\int_0^\eta \eta \frac{\partial w}{\partial z}\, d\eta. \tag{16}$$

Now all terms with explicit z dependence, $\partial w/\partial z$ and $\partial R/\partial z$, appear in this equation. The next task is to express them in terms of known quantities.

We shall approximate $\partial w/\partial z$ by forming the quotient $\Delta w/\Delta z$. From the experimental data one observes that the shape of the w velocity profile varies slowly with z. For a small increment Δz in z we may take $w(\eta, z+\Delta z, t) \simeq k w(\eta, z, t)$, where k is an unknown function of z and t. Thus,

$$\frac{\partial w}{\partial z} \simeq \frac{1}{\Delta z}\operatorname{sgn}\left(\frac{\partial w}{\partial z}\right)|(k-1)\, w(\eta, z, t)|.$$

On substituting this expression for $\partial w/\partial z$ into (16) we get

$$u = \frac{\partial R}{\partial z}\left(\eta w - \frac{2}{\eta}\int_0^\eta \eta w\, d\eta\right) - \frac{|k-1|}{\Delta z}\frac{R}{\eta}\int_0^\eta \operatorname{sgn}\left(\frac{\partial w}{\partial z}\right)\eta |w|\, d\eta.$$

Since the pressure gradient $\partial p/\partial z$ is approximately uniform within the cross-section, we may assume $\partial w/\partial z$ does not change its sign within the cross-section. Then sgn $(\partial w/\partial z)$ may be taken outside the integral sign and the unknown factor $|k-1|\operatorname{sgn}(\partial w/\partial z)/\Delta z$ can be determined easily with the help of the boundary conditions (10) and (11). After performing the necessary calculations we obtain

$$u = \frac{\partial R}{\partial z}\left\{\eta w - \frac{2}{\eta}\left(\int_0^\eta \eta w\, d\eta - \frac{\int_0^1 \eta w\, d\eta}{\int_0^1 \eta |w|\, d\eta}\int_0^\eta \eta |w|\, d\eta\right)\right\} + \frac{1}{\eta}\frac{\partial R}{\partial t}\frac{\int_0^\eta \eta |w|\, d\eta}{\int_0^1 \eta |w|\, d\eta}. \tag{17}$$

Since the radius R of the vessel is a function of both z and t the partial derivative $\partial R/\partial z$ is evaluated keeping t constant. Using the customary notation, let us write this derivative as $(\partial R/\partial z)_t$. We may also consider R as a function of z and p, where p in turn is a function of z and t: $R = R(z,t) = R[z, p(z,t)]$. Then we can express the partial derivative $(\partial R/\partial z)_t$ as

$$\left(\frac{\partial R}{\partial z}\right)_t = \left(\frac{\partial R}{\partial z}\right)_p + \left(\frac{\partial R}{\partial p}\right)_z \left(\frac{\partial p}{\partial z}\right)_t.$$

Here the term $(\partial R/\partial z)_p$ represents the variation of R due to the natural taper of artery. If we denote the taper angle of artery at a given location and at a fixed pressure by ψ we have $(\partial R/\partial z)_p = -\tan\psi$. The product $(\partial R/\partial p)_z (\partial p/\partial z)_t$ expresses the arterial taper generated by the pressure wave and is equal to $-\rho F(\partial R/\partial p)_z$. Putting everything together and dropping subscripts we get

$$\frac{\partial R}{\partial z} = -\left(\tan\psi + \rho F \frac{\partial R}{\partial p}\right).$$

Substituting this relation into (17) we obtain

$$u = -\left(\tan\psi + \rho F \frac{\partial R}{\partial p}\right)\left\{\eta w - \frac{2}{\eta}\left[\int_0^\eta \eta w\, d\eta - \frac{\int_0^1 \eta w\, d\eta}{\int_0^1 \eta |w|\, d\eta}\int_0^\eta \eta |w|\, d\eta\right]\right\} + \frac{1}{\eta}\frac{\partial R}{\partial t}\frac{\int_0^\eta \eta |w|\, d\eta}{\int_0^1 \eta |w|\, d\eta}. \tag{18}$$

This expression for u satisfies the boundary condition (10), and u goes to zero as η goes to zero. When w is uniformly positive or negative within the cross-section at a given time, the expression in square brackets vanishes. The derivative $\partial R/\partial p$ can be determined from the experimental pressure–radius relation. The angle ψ also has to be determined experimentally. At a given location ψ may vary with pressure and, since this is a small angle, it is hard to measure such changes. In our calculations we assumed ψ to be a constant.

3. Finite-difference equations

As a result of simplifications introduced in the previous section, the problem of solving for the velocity components u and w is reduced to integrating (15) and (18) subject to the boundary conditions (11) and (12). We shall carry out this integration by a finite-difference method. Let us consider a rectangular mesh formed by the points of intersection between two families of parallel straight lines:

$$\eta = i\,\delta\eta, \quad i = 0, 1, 2, \ldots, n, \quad n\,\delta\eta = 1,$$

$$\tau = j\,\delta\tau, \quad j = 0, 1, 2, \ldots, s, \quad s\,\delta\tau = 1,$$

where $\tau = t/T$ is the normalized time with respect to the cardiac period T. Here $\delta\eta$ and $\delta\tau$ represent incremental steps in η and τ, respectively. The selection of their values is governed by the consideration of precision and stability of the solution to be attained, as well as the computer time. In computations, it is necessary to choose $\delta\eta$ and $\delta\tau$ so that the equivalent radial velocity of the numerical operation expressed by $R\,\delta\eta/T\,\delta\tau$ is greater than the radial diffusion velocity of the laminar boundary layer expressed as $2(\nu/T\,\delta\tau)^{\frac{1}{2}}$.

By introducing appropriate finite-difference expressions for different derivatives, we obtain the following difference equation for (18) valid at each node (i,j):

$$u_{i,j} = -\left[\tan\psi + \rho F_j\left(\frac{\partial R}{\partial p}\right)_j\right]\left\{i\,\delta\eta\, w_{i,j} - \frac{2}{i\,\delta\eta}\left[U(i,j) - \frac{U(n,j)}{\bar{U}(n,j)}\bar{U}(i,j)\right]\right\} + R'_j\frac{U(i,j)}{i\,\delta\eta\,\bar{U}(n,j)}, \tag{19}$$

where

$$R'_j = \frac{R_{j+1} - R_{j-1}}{2T\,\delta\tau}, \quad U(i,j) = \int_0^{i\delta\eta} \eta w_j\, d\eta, \quad \bar{U}(i,j) = \int_0^{i\delta\eta} \eta |w_j|\, d\eta.$$

The corresponding finite-difference equation for (15) can be expressed as

$$\frac{w_{i,j+1}-w_{i,j}}{T\,\delta\tau} = F_j + \left(\frac{i\,\delta\eta\,R_j'-u_{i,j}}{R_j}+\frac{\nu}{i\,\delta\eta\,R_j^2}\right)\frac{w_{i+1,j}-w_{i-1,j}}{2\delta\eta}$$
$$+\left(\frac{u_{i+1,j}-u_{i-1,j}}{2\delta\eta}+\frac{u_{i,j}}{i\,\delta\eta}\right)\frac{w_{i,j}}{R_j}+\frac{\nu}{R_j^2}\frac{w_{i+1,j}-2w_{i,j}+w_{i-1,j}}{(\delta\eta)^2}. \quad (20)$$

We have indicated at the end of § 2.3 that $u = 0$ at $\eta = 0$; therefore, $u_{0,j} = 0$ for all j. Also, at $\eta = 0$ equation (15) has singularity, hence it must be modified for the numerical operation. Because both w and u are axially symmetric functions, it can be shown that

$$\lim_{\eta\to 0}\frac{1}{\eta}\frac{\partial w}{\partial \eta} = \left.\frac{\partial^2 w}{\partial \eta^2}\right|_{\eta=0}, \quad \lim_{\eta\to 0}\frac{u}{\eta} = \left.\frac{\partial u}{\partial \eta}\right|_{\eta=0}.$$

Therefore, for $i = 0$ equation (20) reduces to

$$\frac{w_{0,j+1}-w_{0,j}}{T\,\delta\tau} = F_j + \frac{4u_{1,j}-u_{2,j}}{\delta\eta}\frac{w_{0,j}}{R_j}+\frac{4\nu}{R_j^2}\frac{w_{1,j}-w_{0,j}}{(\delta\eta)^2}. \quad (21)$$

The last term of (21) is obtained through the condition of axial symmetry, equation (12).

With these equations computation starts with $w_{i,0} = 0$. Then the values of R_j and R_j' are calculated from the experimental data. Next $u_{i,0}$ is computed and the results of these calculations together with the experimental data for the pressure gradient are fed into (20) and (21) to determine $w_{i,1}$. After this, the computation cycle is repeated to obtain $u_{i,1}$ and $w_{i,2}$, $u_{i,2}$ and $w_{i,3}$, etc. It will take the solution a few cardiac cycles to settle into a steady periodic flow.

4. Experiments and numerical results

The theory developed in the previous section contains many parameters which have to be well defined before the validity of the theory can be checked with experiments *in vivo*. However, it is extremely difficult to carry out all the necessary measurements and obtain a consistent set of data within the time during which an animal can be maintained in a steady physiological state. In view of this, we decided to use the model of a circulatory system, which has been under construction in our laboratory, to test the theory. Both the flow field and the physiological parameters of this system can be controlled and measured with greater precision.

The model system is shown in figure 1 (plate 1). This model is designed to simulate the systemic circulation of a medium-sized dog. It consists of the left atrium, left ventricle, aorta, innominate arteries, mesentric arteries, renal arteries and common iliac arteries. The peripheral vascular bed is simulated by long small-lumen elastic tubes. Both the mitral and aortic valves are designed to have dynamic characteristics approximating those of their living counterparts. A glycerin–water mixture with kinematic viscosity $\nu = 0{\cdot}036\,\mathrm{cm^2/s}$

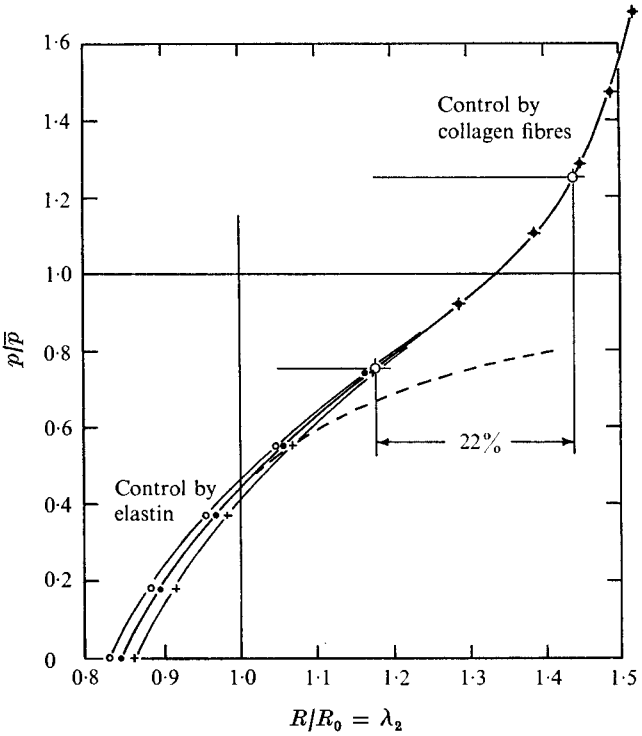

FIGURE 2. Typical pressure–radius response curve for the descending aorta of a dog. $\bar{p}$ = 100 mm Hg, R_0 = 0·50 cm, h_0 = 0·07 cm. o, λ_1 = 1·45; •, λ_1 = 1·40; +, λ_1 = 1·35.

is used as the test fluid. The system, with the help of electronic controls, is capable of producing programmed pressure wave forms, see Ling *et al.* (1969) and Ling (1970).

To construct the model we have studied the elastic response of arteries in detail. In the following we shall discuss the large-deformation characteristics of arteries that we have learned through these studies, and we shall give a short account of our efforts to design model arteries which duplicate these characteristics.

4.1. *Modelling of the arteries*

A typical elastic response curve of the descending aorta of a dog is shown in figure 2. In this figure the arterial pressure p normalized by the mean systemic pressure $\bar{p}$ is plotted versus the radial extension ratio $\lambda_2 = R/R_0$. Here R_0 represents the undeformed value of the inner radius of the artery. Arteries are normally under initial longitudinal strains having an extension ratio $\lambda_1 = l/l_0$ approximately equal to 1·4, where l and l_0 represent the *in vivo* and undeformed lengths of a piece of artery, respectively. At zero pressure and $\lambda_1 = 1{\cdot}4$ the value of λ_2 is approximately 0·85. As pressure rises from this level towards $p/\bar{p} = 0{\cdot}6$, the slope of the curve decreases rapidly. This nonlinear behaviour, which is known as 'ballooning effect' (readily observed during the inflation of toy balloons), is

responsible for the large dynamic capacitance of arteries. Within this pressure range the response of arteries is essentially controlled by highly elastic elastin lamellae, see Wolinsky & Glagov (1964); the relatively stiff collagen fibres, which are in a highly corrugated state, do not contribute to the elastic response. At higher pressure levels ($p/\bar{p} > 0{\cdot}6$) the collagen fibres begin to straighten out and finally bear the major part of the pressure load. This is indicated by the rapid steepening of the pressure–radius curve for $\lambda_2 > 1{\cdot}4$.

At low pressure levels, the pressure–radius curves corresponding to longitudinal extension ratios $\lambda_1 = 1{\cdot}35$ and $1{\cdot}45$ lie below and above the curve for $\lambda_1 = 1{\cdot}4$, respectively. As pressure increases, these three curves gradually merge to a single curve, which indicates a lack of strong elastic coupling between the circumferential and longitudinal strains. Therefore, one must conclude that the collagen fibres are oriented mainly in the circumferential direction. This observation is in agreement with the results obtained through electron microscopy of the arterial walls frozen at various levels of strains, see Wolinsky & Glagov (1964).

Under normal physiological conditions the systemic pressure pulsates approximately within the range $p/\bar{p} = 0{\cdot}75$–$1{\cdot}25$. This corresponds to a 22 % change in the radial extension (see figure 2) or a 49 % change in the cross-sectional area. It is obvious that these large variations in radius and area will have a strong effect on the flow characteristics of arteries.

With this basic knowledge of the arterial structure one may proceed to simulate the overall pressure–radius relation by means of a composite structure of silicone-rubber and corrugated nylon fibres. Since the elastic properties of silicone rubber (a highly elastic and incompressible material) are similar to those of elastin, one may design a silicone-rubber tube to duplicate the behaviour of an artery within the low-pressure range. The pressure–radius relation of such a tube would be governed by the following equation, which is derived from a more general expression given in Green & Adkins (1960):

$$p = \frac{2h_0}{R_0}\left(1 - \frac{1}{\lambda_2^4 \lambda_1^2}\right)\left(\frac{\partial W}{\partial \mathrm{I}} + \lambda_1^2 \frac{\partial W}{\partial \mathrm{II}}\right). \tag{22}$$

Here W denotes the strain energy function of the material, I and II represent the first and second strain invariants, respectively, and h_0 and R_0 are the thickness and inner radius of the undeformed tube, respectively.

The values of the derivatives $\partial W/\partial \mathrm{I}$ and $\partial W/\partial \mathrm{II}$ can be determined by inflating a piece of tube with two different longitudinal extensions. Experiments carried out both on tubes and pieces of arteries (see Ling 1970) indicate that within the physiological range of deformations these derivatives are constant. For elastin values of $\partial W/\partial \mathrm{I}$ and $\partial W/\partial \mathrm{II}$ are $0{\cdot}50$ and $-0{\cdot}05\,\mathrm{kg/cm^2}$, respectively; the corresponding values for G.E. RTV-108 silicone rubber (aged approximately one month) are $2{\cdot}03$ and $-0{\cdot}44\,\mathrm{kg/cm^2}$, respectively.

Since the constancy of the derivatives $\partial W/\partial \mathrm{I}$ and $\partial W/\partial \mathrm{II}$ for rubber (within the range of extensions of the present problem) is an established fact (see Green & Adkins 1960) the above-stated experimental observations have two important implications: (i) elastin may be considered as a rubber-like material, (ii) the lower part of the normalized elastic response curve corresponding to a given λ_1

is a universal curve. To prove the latter statement we first differentiate (22) with respect to R and obtain

$$\frac{dp}{dR} = \frac{8h_0}{R_0^2\lambda_2^5\lambda_1^2}\left(\frac{\partial W}{\partial \mathrm{I}} + \lambda_1^2\frac{\partial W}{\partial \mathrm{II}}\right). \tag{23}$$

Then, we eliminate the factor $(\partial W/\partial \mathrm{I} + \lambda_1^2 \partial W/\partial \mathrm{II})$ between (22) and (23). This gives us

$$\frac{d(p/\bar{p})}{(p/\bar{p})} - \frac{4d\lambda_2}{\lambda_2^5\lambda_1^2 - \lambda_2} = 0. \tag{24}$$

Equation (24) is the differential equation of the elastic response curve. It does not contain any parameter related to the material properties, thus its integral is a universal curve. That is, for a fixed λ_1 and for a given pair $(p/\bar{p}, \lambda_2)$ there is only one elastic response curve for all rubber-like materials. The plot of this curve for $\lambda_1 = 1{\cdot}4$ is shown as the dashed line on figure 2. For $p/\bar{p} < 0{\cdot}5$ it coincides with the corresponding experimental curve. The rapidly decreasing slope of the upper part of this universal curve indicates the fact that without the interference of the collagen fibres arteries would become unstable.

To simulate a given artery in the lower pressure range with a silicone-rubber tube one must know the values of R_0 and h_0. The value of R_0 for the tube should be equal to the undeformed inner radius of the artery. However, R_0 cannot be measured directly. One either may determine its value by extrapolating the experimental pressure–radius curve or calculate it with the help of the following equation, which is obtained by rearranging (24):

$$R_0 = R\lambda_1^{\frac{1}{2}}\left(\frac{4p}{R}\frac{dR}{dp} + 1\right)^{-\frac{1}{4}}. \tag{25}$$

The value of R_0 can be easily obtained by specifying the values of R and dR/dp at a given pressure p together with the value of λ_1. Knowing R_0, one can find h_0 from (22). Since rubber is stiffer than elastin, the undeformed thickness of the tube will be smaller than the corresponding thickness of the artery.

To fabricate the rubber tube, we used a teflon-coated mandrel whose dimensions were the same as the internal dimensions of the undeformed artery. The silicone rubber is applied and cured over the mandrel in successive layers approximately 0·01 cm thick until the required distribution for h_0 is obtained. To prevent the unsymmetrical ballooning effect, the circumferential variation of the thickness should be kept within $\pm$ 0·003 cm.

To simulate the elastic characteristics of arteries in the higher pressure range we use the fibres of regular nylon stockings (the type which runs). A piece of this knitted material is mounted over a rigid frame. Then, for every six rows of the knitting we remove the interconnecting loops from five rows leaving one row intact. The result is a system of free corrugated fibres interconnected with each other at every sixth corrugation. This material is impregnated with silicone rubber and wrapped (in a fully stretched state) around the tube, which has been previously slipped over a new mandrel having dimensions corresponding to $\lambda_2 = 1{\cdot}5$. The fibre system is then bonded to the tube along the knitted rows leaving the corrugated parts free. Figure 3 shows the composite tube in its strained and unstrained states.

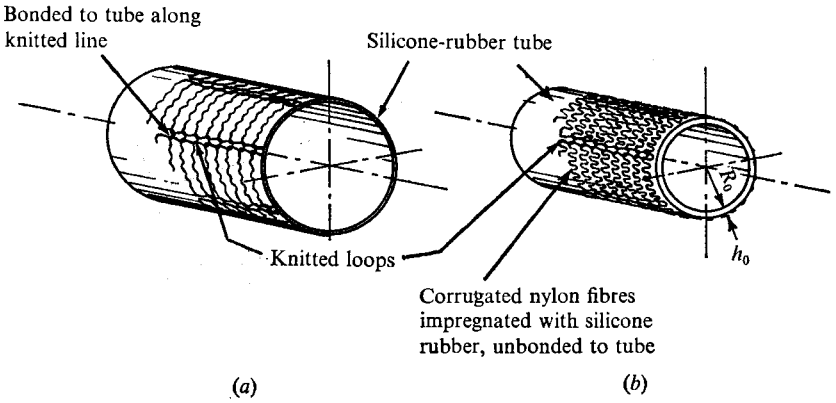

FIGURE 3. Model artery (*a*) a fully strained and (*b*) an unstrained state.

4.2. *Measurements*

We have chosen the middle descending thoracic aorta of the model as the test site. This portion of the aorta is straight and is free from large arterial branches. At this location we have measured the pressure, pressure gradient, pressure–radius relation, wall taper, axial velocity profiles and wall shear. The first four of these measurements are used as the input information for the computations.

To provide the necessary precision for the measurement of the pressure gradient a new technique was developed. In this technique, two matched Statham P23Db pressure transducers are used together with a duplex three-way valve for transposing the inlet of each transducer to either one of the three pressure taps on the aorta. One of the taps on the aorta is located at the point where the local flow characteristics are to be determined. The other two taps are located 2·5 cm proximal and 2·5 cm distal to this point, respectively. For measuring the pressure as well as for checking the static and dynamic matching of the two pressure gauges, the inlets of the transducers are connected through the duplex three-way valve to a common catheter. This catheter is first connected to a known static pressure source, with which we calibrate and adjust the two gauges until their outputs track one another for all pressures ranging from 0 to 140 mm Hg. The common catheter is then transferred to the central tap of the pulsating aorta. The two dynamic pressure signals from the transducers are subtracted from one another through a precision operational amplifier. For a well-balanced system this difference should not exceed $\pm 0{\cdot}5$ mm Hg. If the difference exceeds these limits, the cause can usually be traced either to micro gas bubbles trapped in the system or to catheters which are not stiff enough. The bubbles can be eliminated by soaking the system overnight in de-aerated saline, see Barnett, Greenfield & Fox (1961). When a satisfactory dynamic balance is achieved, the pressure signal from one of the gauges is recorded on a calibrated frequency-modulated tape.

To obtain the pressure gradient signal, the inlets of the first and second transducers are connected through the duplex three-way valve to the proximal and the distal pressure tap on the aorta, respectively. By subtracting the signal

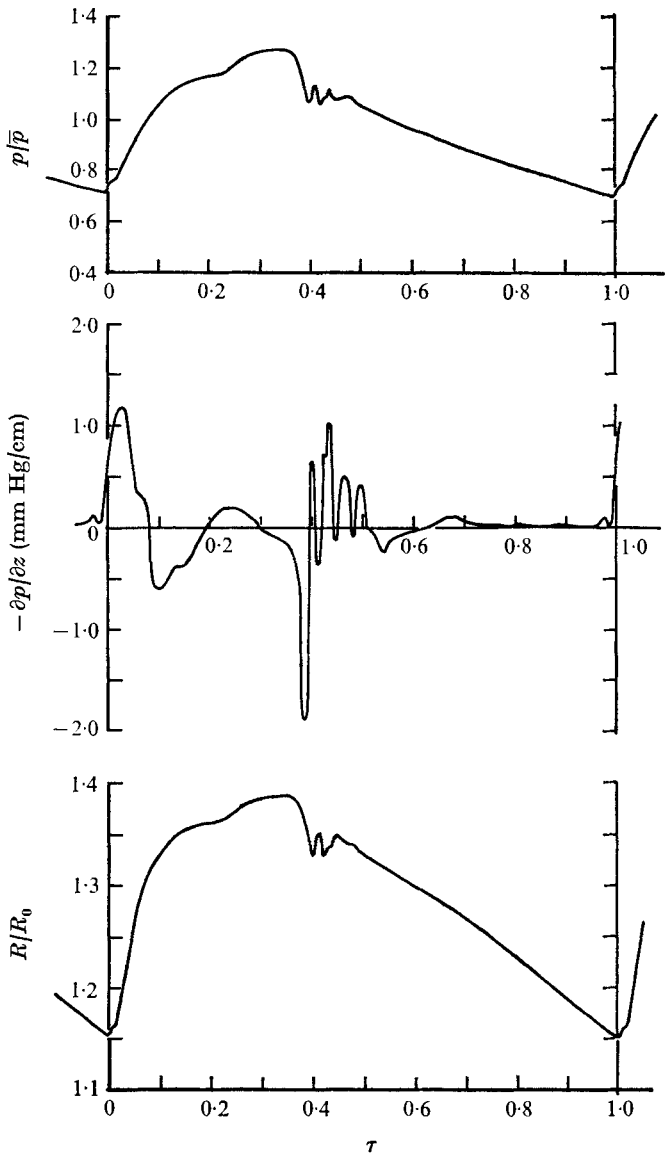

FIGURE 4. Pressure, pressure gradient and inner radius as functions of the cardiac cycle. $\bar{p} = 100$ mm Hg, $(\overline{-\partial p/\partial z}) = 0{\cdot}023$ mm Hg/cm, $R_0 = 0{\cdot}47$ cm.

of the first transducer from that of the second transducer through the operational amplifier, we obtain the 'forward' pressure difference. Similarly, by reversing the pressure connexions through the duplex three-way valve we obtain the 'backward' pressure difference. These signals are recorded successively on the tape for a minimum of 30 cardiac cycles. Since both the magnitude and sign of the static instrument errors in these measured signals do not change under the above described transposition of the pressure connexions (the signs of the real signals will change), the static measurement errors are eliminated by subtracting

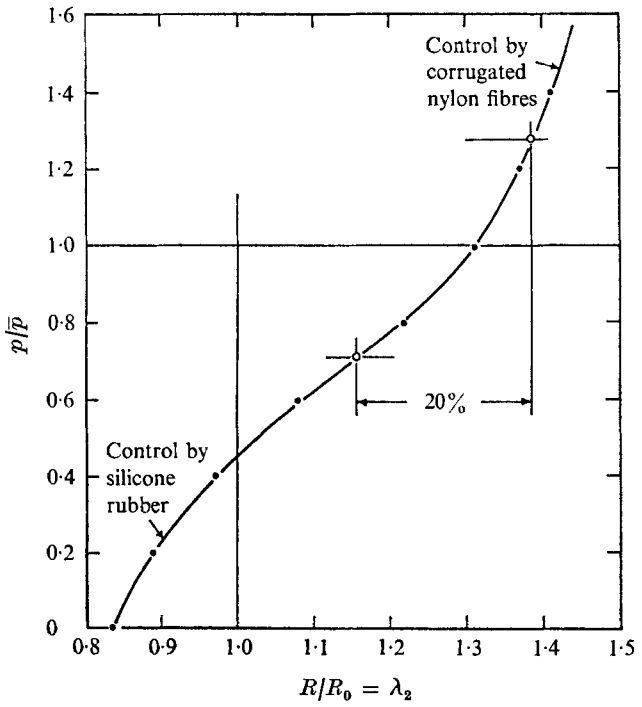

FIGURE 5. Pressure–radius response curve for the descending aorta of the model for $\lambda_1 = 1{\cdot}4$. $\bar{p} = 100$ mm Hg, $R_0 = 0{\cdot}47$ cm, $h_0 = 0{\cdot}025$ cm, $\psi = 0{\cdot}5°$.

the 'backward' from the 'forward' pressure difference signal. In order to preserve the required precision this operation is performed by a digital computer. The resulting signal, which is twice the true pressure difference, is divided by twice the distance between the two outer pressure taps and averaged over 15 cardiac cycles to obtain the pressure gradient wave. With this technique, one can determine the zero datum of the pressure gradient wave to an accuracy of $\pm 0{\cdot}001$ mm Hg/cm. The results of both the pressure and pressure gradient measurements are shown in figure 4.

The pressure–radius relation at the test site of the present model is shown in figure 5. This curve is obtained by photographing simultaneously the inflation of the vessel and the pressure signal using an 8 mm cine camera equipped with a high-power telephoto lens. For a given pressure, the outer radius of the vessel together with the local taper is read from the film with the help of a calibrated microscope. The corresponding inner radius is computed using the property of incompressibility of the vessel wall. From figure 5 we see that the model artery has all the essential elastic characteristics of its living counterpart shown in figure 2.

The axial velocity profiles are measured by a hot-film velocity probe. Both the description of this instrument and the method of measurement have been reported previously (see Ling *et al.* 1968). For the present measurements, a lucite collar padded with a 0·3 cm thick layer of soft foam rubber is used to control the radial position of the probe, see figure 6. The large surface area of the foam

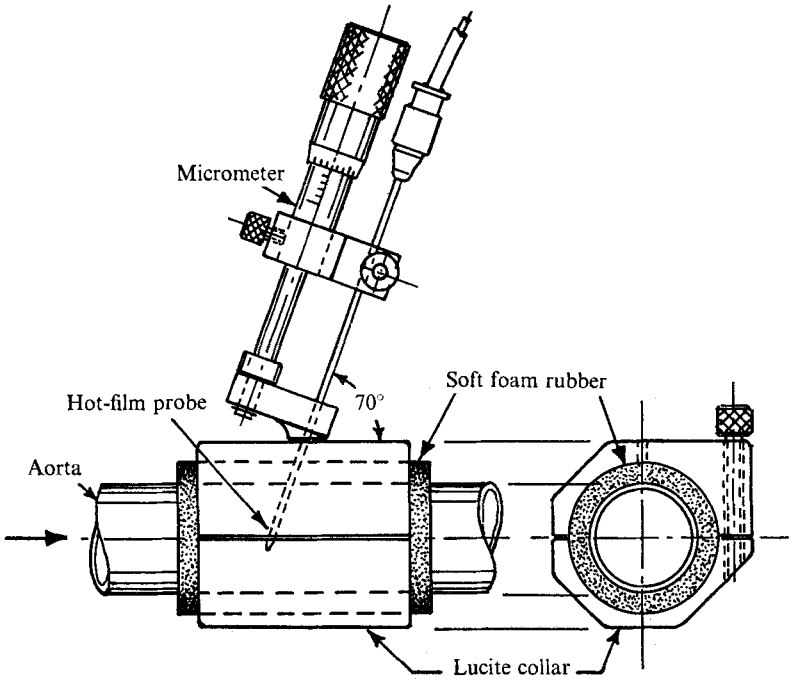

FIGURE 6. Traversing system for the velocity-sensing probe.

rubber helps to maintain concentricity of the collar with respect to the aorta while allowing the vessel to expand freely. The results of the measurements, normalized by the peak centre-line velocity w_m, are plotted as dotted lines for various values of the normalized cardiac time $\tau = t/T$, see figure 7. Here, T represents the cardiac period. The normalized centre-line velocity wave is shown in figure 7(*b*).

The velocity gradient wave at the wall is measured by a hot-film shear probe (see Ling *et al.* 1968) and is shown as the dotted line in figure 8(*a*).

4.3. *Numerical integration and results*

The normalized cardiac cycle is divided into 200 equal steps, i.e. $\delta\tau = 0{\cdot}005$. The measured pressure and pressure gradient waves, shown in figure 4, are both read into the computer as 200 data points. Similarly, the normalized inner radius is divided into 20 equal spaces, i.e. $\delta\eta = 0{\cdot}05$. The elastic response curve, shown in figure 5, is expressed as a seventh-order polynominal in p and is stored in the computer as a subroutine program. Since the effect of the mass of the vessel wall is found to be negligible in the present problem, the motion of the wall is assumed to follow the pressure wave. Therefore, after the inertial term in (4) has been dropped, the value of the inner radius $R(\tau)$ is determined directly through the stored $p(\tau)$ and pressure–radius information.

Both the calculated radial wall velocity wave and the radial velocity profiles are shown in figure 9. It is interesting to note that during systole for $0{\cdot}1 < \tau < 0{\cdot}3$ the u profiles tend to fold towards the negative direction. Near the wall both u

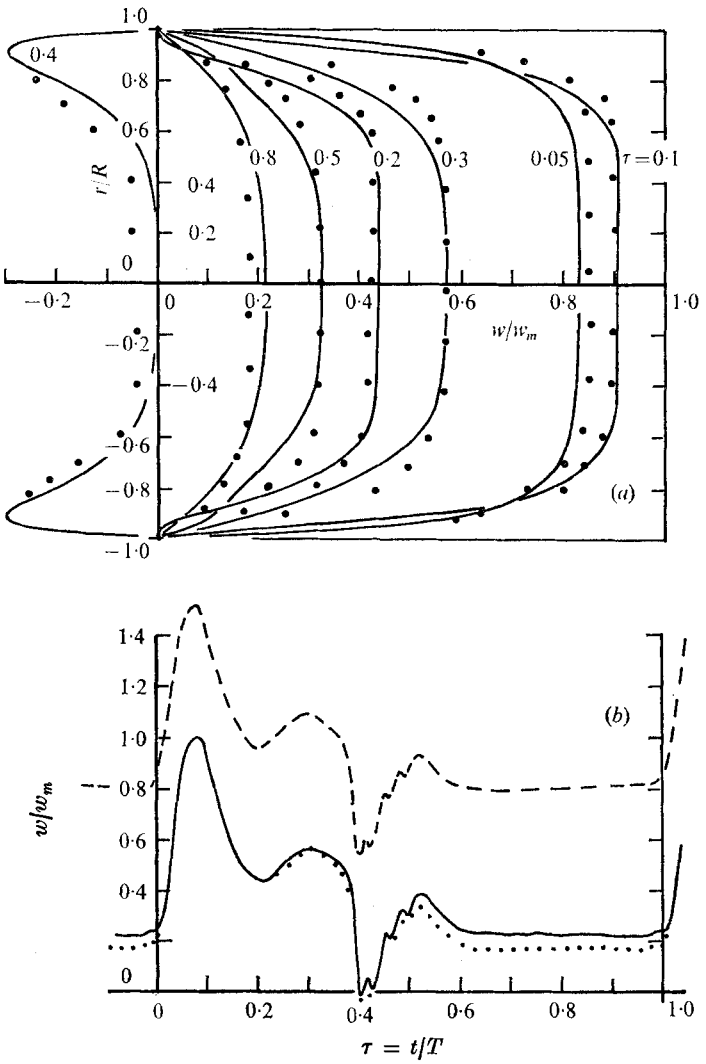

FIGURE 7. (*a*) Axial velocity profiles and (*b*) centre-line velocity wave. (*a*) —, theory; ····, experiment. (*b*) —, nonlinear theory; – – –, linear theory; ····, experiment. $w_m = 77$ cm/s, $T = 0{\cdot}8$ s, $r = 0$.

and $\partial u/\partial r$ are positive, and for $\eta < 0{\cdot}6$ the reverse is true. This behaviour is related to the arterial taper; without the taper the profiles would have the opposite tendency. The resultant effect of this is to accelerate flow axially near the wall and decelerate it within the central core; see the third term on the right-hand side of (15). Even though the magnitude of u is small in comparison with the peak centre-line velocity w_m, it is directly responsible for the local storage of blood and is manifest in the convective acceleration.

The calculated axial velocity profiles and the centre-line velocity wave are shown in figure 7. The agreement between the computed and the measured values is good. Near the wall, the predicted values of the velocity are smaller than the

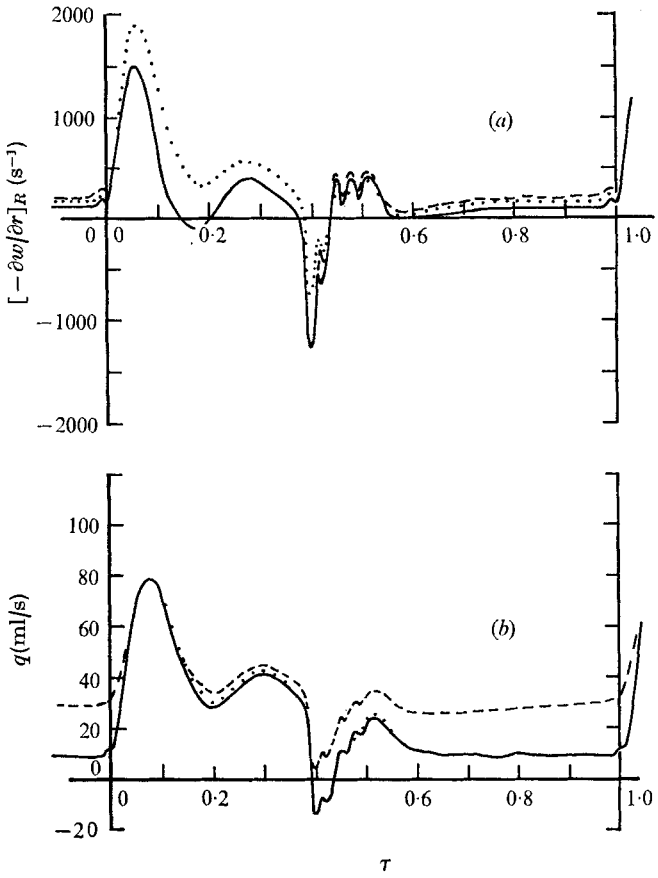

FIGURE 8. (*a*) Wall shear and (*b*) discharge waves as functions of the cardiac cycle. (*a*) —, mean pressure gradient due to wall shear = 0·015 mm Hg/cm, from theory; ····, experiment. (*b*) —, nonlinear theory; – – –, linear theory; ····, experiment. Q = 18·4 ml/stroke.

measured ones. The corresponding theoretical and experimental discharge waves are shown in figure 8(*b*) and are obtained by integrating the calculated and measured velocity profiles. The agreement between these two curves is very good.

The computed velocity gradient at the wall is shown in figure 8(*a*). During systole the measured values of the wall shear are higher than the computed ones.

5. Comparison with linear theory

In a previous publication, Ling *et al.* (1969) reported velocity profiles and wall shears measured in an elastic tube and compared them with those predicted by the linear theory. The calculations were based on the theory given by Atabek (1968), using the measured values of the centre-line velocity as the input data. The predicted velocity profiles are less blunt during systole and have large negative parts near the wall during diastole. Consequently the wave form of the predicted wall shear is significantly different from the measured one.

One may also use the pressure gradient data as an input in the linear theory

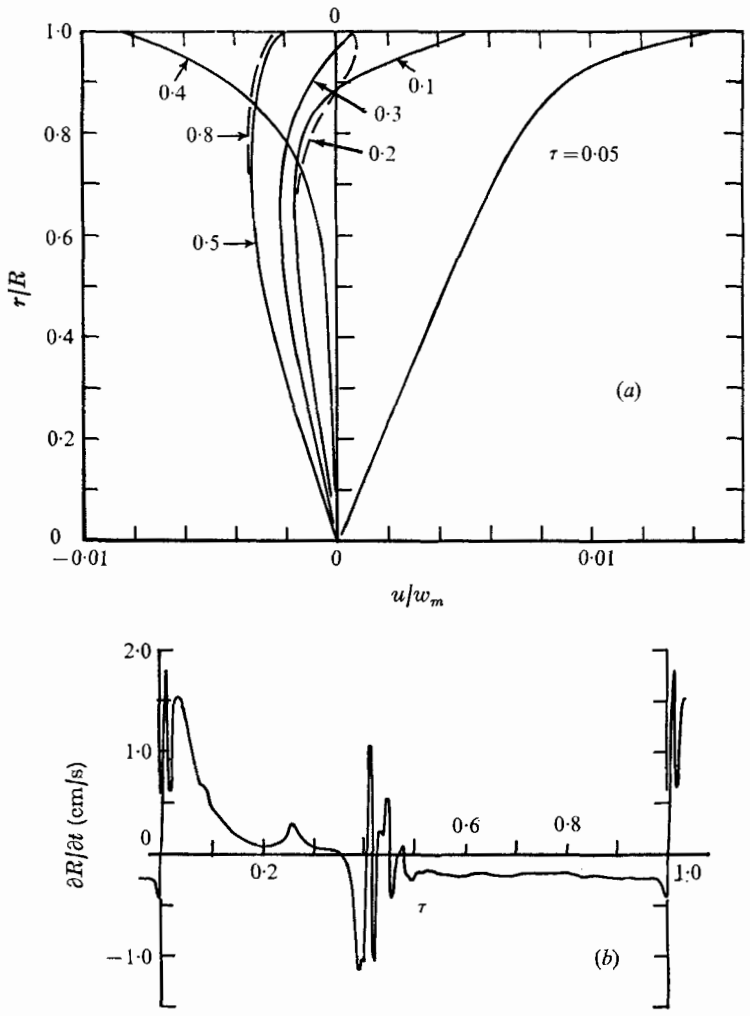

FIGURE 9. (*a*) Radial velocity profiles and (*b*) velocity of wall as function of the cardiac cycle.

for calculating the flow. We have used the pressure gradient given in figure 4 to calculate the axial velocity profiles, wall shear and discharge rate in the model artery. The calculated velocity profiles differ significantly from the measured ones. During systole their forms are essentially parabolic. The magnitude of the maximum centre-line velocity is approximately 50 % larger than the corresponding measured value. Because of their large magnitudes, we have decided not to show these profiles in figure 7. However, the centre-line velocity wave is shown as the dashed line in figure 7 (*b*); except for the large mean flow component, this curve is very similar to the measured wave. The wave of wall shear predicted by the linear theory is very close to the one predicted by the nonlinear theory and is depicted as the dashed curve in figure 8 (*a*). The calculated discharge wave is shown as the dashed curve in figure 8 (*b*). Although it agrees fairly well with

the measured discharge wave during systole, the predicted values are too high during diastole.

Since in the linear theory a small change in the mean pressure gradient would produce a large difference in the mean flow, a slight adjustment in the measured pressure gradient could easily make the predicted discharge wave agree with the measured one. This observation, while emphasizing the need for a precise pressure gradient measurement, explains the apparent agreement of the measured and predicted discharge waves given by previous investigators, see MacDonald (1960). The reason for the failure of the linear theory in predicting acceptable velocity profiles lies in the process of linearization. As one can see from (2), the longitudinal pressure gradient is balanced by the inertia forces due to both local and convective accelerations as well as by the viscous forces generated by velocity gradients. In the linearization process the convective acceleration terms are dropped. As a consequence, the linearized equations are forced to produce the required balance by artificially increasing viscous forces with higher flow rates. For the case under consideration, the linear theory predicts a large discharge rate of 32 ml./stroke, while the corresponding figures obtained from the non-linear theory and the measurements are 17·9 and 18·4 ml./stroke, respectively.

6. Concluding remarks

From the experimental data on the aortas of eight dogs, which were subjected to strain rates within the physiological range, we were not able to detect in these arteries any measurable viscoelastic behaviour. Therefore, in the present work there is no explicit reference to the viscoelastic behaviour of the arteries. The arteries which show serious viscoelastic behaviour will have hysteresis loops on their elastic response curves. Such response characteristics can be readily stored in the computer and used with the present theory.

In view of frequent arterial branching, input information introduced at the root of aorta is gradually lost as the flow progresses along the vessel. A theory taking into account all branching effects would be extremely complex. Therefore, a simpler theory (like the one presented above) which uses local information to predict the local flow is the only alternative available at this time. We hope that this technique may prove to be useful not only for conducting controlled study of the various biomedical problems associated with the haemodynamic events, but also for various clinical applications. Measurement of the pressure gradients through a double-lumen catheter, instead of direct arterial taps, should enhance the applicability of this technique for clinical diagnostic work.

The authors would like to take this opportunity to express their appreciation to Dr D. L. Fry and Dr D. J. Patel of the National Heart and Lung Institute for their continuous encouragement and generous help in the course of this work. They also gratefully acknowledge the assistance of Dr T. T. Huang of the U.S. Naval Ship Research and Development Centre for the numerical work. This research has been supported by the U.S. Public Health Service under Grant HE 12083-04 and by N.A.S.A. under Grant NGL-09-005-067.

REFERENCES

ATABEK, H. B. 1968 *Biophys. J.* **8**, 626.

BARNETT, G. O., GREENFIELD, J. C. & FOX, S. M. 1961 *Am. Heart J.* **62**, 359.

COX, R. H. 1969 *J. Biochem.* **2**, 251.

FRY, D. L., GRIGGS, D. M. & GREENFIELD, J. C. 1964 *Pulsatile Blood Flow* (ed. E. O. Attinger), p. 101. McGraw-Hill.

GREEN, A. E. & ADKINS, J. E. 1960 *Large Elastic Deformations*, ch. 4. Oxford University Press.

LING, S. C. 1970 *A.I.A.A. Paper*, no. 70–789.

LING, S. C., ATABEK, H. B. & CARMODY, J. J. 1969 *Proc. 12th Cong. of Appl. Mech.* p. 277. Springer.

LING, S. C., ATABEK, H. B., FRY, D. L., PATEL, D. J. & JANICKI, J. S. 1968 *Circulation Res.* **23**, 789.

MCDONALD, D. A. 1960 *Blood Flow in Arteries*, ch. 5. Williams & Wilkins.

PATEL, D. J., GREENFIELD, J. C. & FRY, D. L. 1964 *Pulsatile Blood Flow* (ed. E. O. Attinger), p. 293. McGraw-Hill.

WOLINSKY, H. & GLAGOV, S. 1964 *Circulation Res.* **14**, 400.

WOMERSLEY, J. R. 1957 An elastic tube theory of pulse transmission and oscillatory flow in mammalian arteries. *Wright Air Dev. Ctr. Tech. Rep.* WADC-TR-56-614.

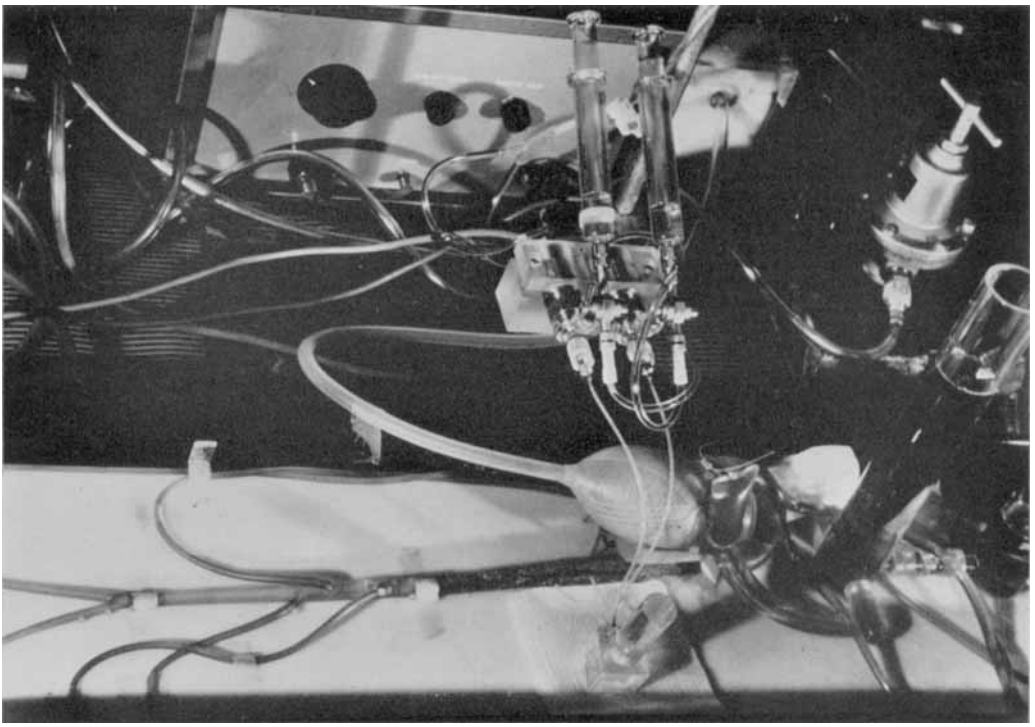

FIGURE 1. Model circulatory system. The duplex three-way valve and pressure gauges are located in front and at the top of the model heart, respectively.